

# The Impact of Grain-size Distributions on Magnetic Measurements

Frenk Out<sup>1</sup>, Rosa A. de Boer<sup>1</sup>, John Walmsley<sup>2</sup>, Lennart V. de Groot<sup>1</sup>

<sup>1</sup>Paleomagnetic laboratory Fort Hoofddijk, Department of Earth Sciences, Utrecht University,  
Budapestlaan 17, 3584 CD Utrecht, The Netherlands.

<sup>2</sup>Department of Materials Science & Metallurgy, University of Cambridge, 27 Charles Babbage Road, CB3  
0FS Cambridge, United Kingdom.

## Key Points:

- We determine contributions of individual magnetic carriers to bulk magnetic measurements and surface magnetometry
- Measurements on bulk samples are sensitive to small grains ( $<200$  nm); surface magnetometry emphasises signals from larger grains ( $>1$   $\mu\text{m}$ )
- Our observations explain why undetected ghost grains in MMT experiments have an unintuitively low impact on the accuracy of MMT results

## Abstract

Magnetic signals in igneous rocks arise from assemblages of iron-oxide bearing minerals that differ in e.g. size, shape, and chemistry. Paleomagnetic measurements on bulk samples measure millions of such grains simultaneously, producing a statistical ensemble of the magnetic moments of the individual minerals. Scanning magnetometry techniques such as the Quantum Diamond Microscope (QDM) measure magnetic signals on micrometer scales, allowing the identification of magnetic moments of individual grains in a sample using e.g. Micromagnetic Tomography (MMT). Here we produce a grain-size distribution of iron-oxides in a typical Hawaiian basalt from the superparamagnetic threshold ( $\sim 40$  nm) to grains with a diameter of  $10\ \mu\text{m}$ . This grain-size distribution is obtained by combining FIB-SEM and MicroCT data from sister specimens, and normalizing them to the mineral surface area of non-magnetic minerals. Then we use this grain-size distribution to determine the contributions of individual magnetic carriers to bulk magnetic measurements and surface magnetometry. We found that measurements on bulk samples are sensitive to relatively small grain sizes in the realm of single domain or vortex states ( $< 200$  nm), while signals in surface magnetometry arise mainly from larger grains with diameters  $> 1\ \mu\text{m}$ . This implies that bulk measurements cannot be compared straightforwardly to signals from surface magnetometry from the same sample. Moreover, our observations explain why MMT results are insensitive to the presence of many small grains in a sample that intuitively should hamper their outcome.

## Plain Language Summary

Magnetic grains in lavas obtain a magnetic signal while cooling in presence of Earth's magnetic field. However, not all grains store the signal well, meaning that both good and bad recorders are present. Classical paleomagnetic techniques measure the magnetic signal of all recorders together, i.e. the bulk signal. New scanning magnetometry techniques such as Micromagnetic Tomography acquire the signal from individual recorders in the lava, enabling selecting only the good recorders and rejecting the signal of bad recorders. Here we found that these two types of magnetic measurements do not measure the same grains that are present in the sample: classical techniques emphasize small grains ( $< 200$  nm), while signals in surface magnetometry arise mainly from larger grains with diameters  $> 1\ \mu\text{m}$ . This means that measurements from both techniques done on the same sample material cannot be compared straightforwardly. Furthermore, our results explain

47 why Micromagnetic Tomography results often are successful, even when many small mag-  
48 netic grains that intuitively should hamper this technique are present in a sample.

## 1 Introduction

The past state of the Earth’s magnetic field is recorded by iron-oxide bearing minerals such as (titano-)magnetite when they cool, e.g. when igneous rocks are formed. When these iron-oxides cool down below their Curie temperature, they acquire a thermo-remanent magnetization (TRM) that relates to the magnetic field present during cooling. These TRMs are important archives of the past behavior of the Earth’s magnetic field (e.g. Dunlop & Özdemir, 1997; Tauxe & Yamazaki, 2015).

Not all iron-oxide bearing grains, however, store magnetic information well. The magnetic state of an iron-oxide grain after cooling depends on many factors. Some iron-oxides therefore carry a magnetization that does not correspond to the paleomagnetic field anymore, or their magnetization changes over time – thereby losing the paleomagnetic information stored in them. Also, the magnetic behavior of iron-oxides during reheating experiments may lead to ambiguous results. This is one of the reasons why paleointensities are difficult to recover from bulk samples: only 10 to 20% of all paleointensity experiments pass sufficient selection criteria and yield interpretable results (e.g. Tauxe & Yamazaki, 2015; Nagy et al., 2017).

The iron-oxide grains in volcanic rocks are assemblages of grains that differ in size, shape, and chemistry. Some of them may be reliable recorders of the Earth’s magnetic field, and others may not. To circumvent the problem of measuring signals simultaneously from good and bad recorders, de Groot et al. (2018) proposed a new paleomagnetic technique to obtain magnetic moments of individual iron-oxide grains in a sample: Micromagnetic Tomography (MMT). MMT infers magnetic moments by first acquiring a magnetic surface image of a (cut-out of a) thin-section of a sample using a surface magnetometry technique (e.g. a Quantum Diamond Microscope, QDM: Glenn et al., 2017). Then, the position of each iron-oxide grain in that sample is obtained with X-Ray Micro Computed Tomography (MicroCT). These two pieces of information are combined in a mathematical inversion to retrieve individual magnetic moments by minimizing residuals in the magnetic surface map. Both de Groot et al. (2021) and Kusters et al. (2023) have shown the capabilities of MMT on Hawaiian rock samples. The mathematical uncertainties of the technique have been modeled by Out et al. (2022).

Theoretically, MMT is able to retrieve the magnetic moment of even the smallest stable single domain (SD) iron-oxide grains. These grains are unfortunately often not

detected by present-day MicroCT equipment, because these machines have resolutions down to 350-500 nm. As a grain can only be reliably resolved if it consists of a couple of voxels, it is currently only possible to detect grains with a diameter of  $>1\ \mu\text{m}$ . Consequently, SD and pseudo-single domain (PSD) grains may produce a detectable magnetic signal in the magnetic surface scan, while they do not show up in the MicroCT data. These undetected ‘ghost grains’ are a challenge for MMT, because the method can only deliver unique and reliable results if all measured magnetic signals originate from detected iron-oxides in the sample (Fabian & De Groot, 2019). Currently it is unknown how many small ghost grains are present in (Hawaiian) basaltic lavas (de Groot et al., 2021; Kusters et al., 2023) and more importantly, what their influence on QDM measurements and MMT results exactly is.

To answer these questions, we characterize the distribution of these ghost grains using Focused Ion Beam Scanning Electron Microscopy (FIB-SEM), following the slice-and-view approach of Nikolaisen et al. (2020). With FIB-SEM it is possible to image a rock sample of micrometer size with a resolution of  $\sim 20\ \text{nm}$  by slicing (or milling) through the sample and imaging the cleared surface. In this way, a 3D reconstruction of the sample volume with these previously undetected iron-oxide grains can be reconstructed. Since iron-oxide grains reflect electrons well, these grains are detected through backscattered electron images obtained with scanning electron microscopy. After obtaining these grains, we will use MicroCT data on the same sample material to obtain a grain-size distribution spanning both the nanometer and micrometer scale. Linking these two datasets, however, is not straightforward because iron-oxides are not uniformly present in a rock sample but cluster around large mineral interfaces. We therefore use the surface area of relatively large, non-magnetic, grains in both the FIB-SEM and MicroCT data to normalize and combine the grain-size distributions obtained from both analyses. Once we establish the grain-size distribution for our sample from the superparamagnetic threshold at 40 nm to a grain-size of  $10\ \mu\text{m}$ , we can model the impact of different grain-sizes on magnetic measurements, albeit measurements on bulk sample material, or scanning magnetometry such as the QDM.

We selected a sample from a Hawaiian lava flow for our analyses: a sample from site HW03 (de Groot et al., 2021). Sister specimens from this site were previously used for MMT analyses by de Groot et al. (2021) and Kusters et al. (2023). Moreover, sample material from this site was used in an extensive paleomagnetic study, including dif-

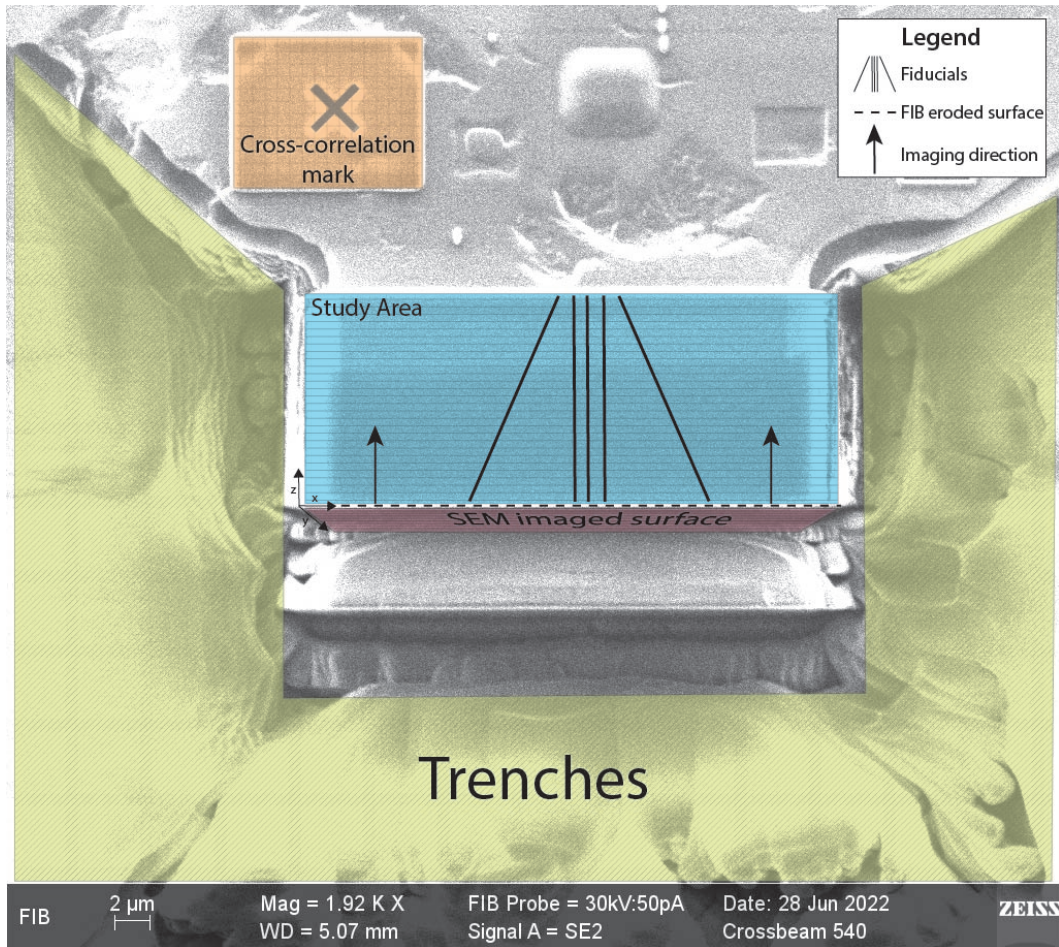


**Figure 1.** Overview of the study area within a Hawaiian basalt examined by slice-and-view through FIB-SEM. After the ion beam removed a 20.18 nm slice from the bottom of the study area, a backscattered and secondary reflected electron image is recorded. Instrumental drift is constrained by calibrating the FIB-SEM every 100 slices using the cross-correlation mark in the top left corner.

ferent paleointensity methods (de Groot et al., 2013), and its properties were studied in-depth by ter Maat et al. (2018). This latter study included chemical, crystallographic and physical techniques such as Scanning Electron Microscopy, Microprobe analyses and Magnetic Force Microscopy.

## 2 Grain-size distribution

Pivotal in obtaining a realistic grain-size distribution is acquiring the volume for all iron-oxide grains present in basaltic rocks. The sample we have used in this study was

taken from the 1907 lava flow from Hawaii, drilled at 20 cm depth measured from the top of the flow (HW03; de Groot et al., 2013; ter Maat et al., 2018). The MicroCT data of this sample had already been studied by de Groot et al. (2021) and Kusters et al. (2023). Petrographic analyses by ter Maat et al. (2018) and Kusters et al. (2023) revealed that the sample material has a typical basaltic composition containing iron-oxides with a cubic shape enveloped by a matrix of glass, plagioclase, and clinopyroxene. All these analyses that were previously done make our sample an ideal and well-controlled reference sample to use for this study.

The MicroCT data of this sample facilitates the detection of iron-oxide grains larger than  $\sim 1 \mu\text{m}$ , but leaves most of the SD and PSD grains undetected. With the help of FIB-SEM (e.g. Einsle et al., 2016; Nikolaisen et al., 2020) we estimate the number of previously undetected SD and PSD grains. Technically, FIB-SEM allows a pixel size of 10 nm and a field of view close to 20 by 20  $\mu\text{m}$ , which enables the detection of both the smallest stable SD grains above the superparamagnetic threshold of 40 nm (Dunlop & Özdemir, 1997) and large MD grains of  $>1 \mu\text{m}$ , which are normally at the lower detection limit of MicroCT.

## 2.1 Image acquisition with FIB-SEM

We applied FIB-SEM on a sample of HW03, following the slice-and-view procedure described in Einsle et al. (2016) and Nikolaisen et al. (2020). First, a 60  $\mu\text{m}$  thick slice with a diameter of 2 mm was extracted from the specimen and coated with a nanometer thick layer of gold. Around the edges of the sample, silver was applied with a toothpick so that electrons could easily pass through the sample. The sample was placed in a Zeiss Crossbeam 540 after which we searched the top of the sample for a 20 x 20  $\mu\text{m}$  area containing many small iron-oxides. This area was prepared for the slice-and-view procedure by first applying a 1  $\mu\text{m}$  thick layer of platinum while maintaining an ion beam current of 700 pA and an accelerating voltage of 30 kV. This accelerating voltage did not change unless explicitly stated otherwise.

Then, five 0.5  $\mu\text{m}$  deep fiducials were engraved with a current of 50 pA (Fig. 1). The three central fiducials were created parallel to each other to enable image alignment during data processing. The outer two fiducials were created under an angle of 25 degrees with respect to the three central fiducials. These two fiducials ensured that the real



thickness of the individual image slices could later be checked. To make these fiducials visible, a 0.6  $\mu\text{m}$  thick carbon layer was deposited on top of the platinum layer with an ion beam current of 700 pA and a dwell-time of 400 seconds. Then, three trenches with a depth of 25  $\mu\text{m}$  and an area of 27 by 46  $\mu\text{m}^2$  were eroded at three sides of the selected area. For this erosion procedure, we used an ion beam current kept at 15 nA with a back-and-forth milling pattern (bidirectional). Using the same bidirectional routine, the current was reduced from 15 nA to 7 nA to create smooth trenches next to the studied area. Instrumental drift during measurements was reduced to a minimum by applying a cross-correlation mark outside the studied area (Fig. 1).

The data acquisition process was initiated after a 20.18 nm slice of the sample area was removed with FIB (beam current at 1.5 nA with an accelerating voltage between 1 to 6 kV). Backscattered and secondary reflected electrons images were obtained using SEM, after which a 20.18 nm layer of sample was removed using FIB. After this procedure was repeated a hundred times instrumental drift was corrected by checking alignment with the cross-correlation mark. After the prepared section had been scanned, 601 gray-scale images of both backscattered and secondary reflected electrons were saved in TIFF format. Each file encompassed a pixel area of 3072 x 2104 pixels with a pixel size of 10.09 nm and a 8-bit gray-scale. The total volume of sample analysed was therefore 31.0 x 21.2 x 12.1  $\mu\text{m}^3$ . Initial investigation of the scanned volume reveals many iron-oxides <1  $\mu\text{m}$  residing on the mineral interfaces of both plagioclase and clinopyroxene (see repository of Out et al., 2023).

## 2.2 Dataprocessing

### 2.2.1 *Extracting grains from FIB-SEM data*

After image acquisition, we aim to retrieve a grain-size distribution from the data. Every data processing step was executed with Python 3 and the OpenCV library (Bradski, 2000) and is freely available (repository of Out et al., 2023); an overview of the results of the individual processing steps can be found in the supplementary information (Fig. S1). We initiated our data processing by loading the 601 backscattered electron images and aligning them using the three parallel fiducials. After alignment, we removed all duplicate images. To remove the effects of both curtaining and the platina and carbon deposited layers, every image was cropped to 2600  $\times$  1000 pixels.



Through denoising and thresholding, SD and PSD iron-oxides could be retrieved from FIB-SEM images as shown by Nikolaisen et al. (2020). First, the background noise of our 549 images was reduced using 2-by-2 pixel binning and a non-local means filter. Because iron-oxide grains have a high density compared to surrounding silicates, we could make use of the large difference in electron reflectivity. These grains could, therefore, be derived from the images by applying a gray-scale thresholding, where after a 3D pixel volume of the individual iron-oxide grains could be obtained. We set a high thresholding value of 220 to retrieve the largest part of the iron-oxides, as lower values would include parts of other minerals (Fig. S1a).

However, the smallest iron-oxide grains are not fully imaged yet, because they are embedded in plagioclase and pyroxene minerals, which have a lower electron reflectivity. The transition between these different reflectivities causes the edges of the iron-oxides to have a lower gray-scale value than their centers, thereby reducing grain volume of these small grains drastically. To quantify the volume of these grains well, the interference of surrounding silicates was taken into account: we expanded the grain-shape of the iron-oxides by lowering the threshold value from 220 to 160. This involves a potential volume overestimation of some grains. Nevertheless, manual inspection of all grain-shapes revealed that the readjusted shapes of the smallest grains followed the overall structures in the images better than the original, strictly thresholded, shapes. Lastly, we removed all iron-oxides that extend beyond the edges of the FIB-SEM domain and recovered 1,558 grains. We calculated the volume of these iron-oxides, and transformed these volumes into equivalent diameters assuming spherical grains. In this study we do not take grain-shape into account.

### 2.2.2 *Scaling FIB-SEM and MicroCT data*

To obtain a grain-size distribution spanning the entire range of naturally occurring iron-oxides, we combined our FIB-SEM data with MicroCT data that was obtained on a sister specimen of HW03 by Kusters et al. (2023). Since iron-oxides in our FIB-SEM dataset are not homogeneously distributed throughout the rock, it is not straightforward to link MicroCT data one-to-one to FIB-SEM data based on volume. The dataset shows that most iron-oxides are positioned on the interface between larger grains (mainly plagioclase and pyroxene); especially the smallest iron-oxides attach themselves to this ‘honeycomb’ structure of other minerals (Fig. 2). Because this honeycomb structure of rel-

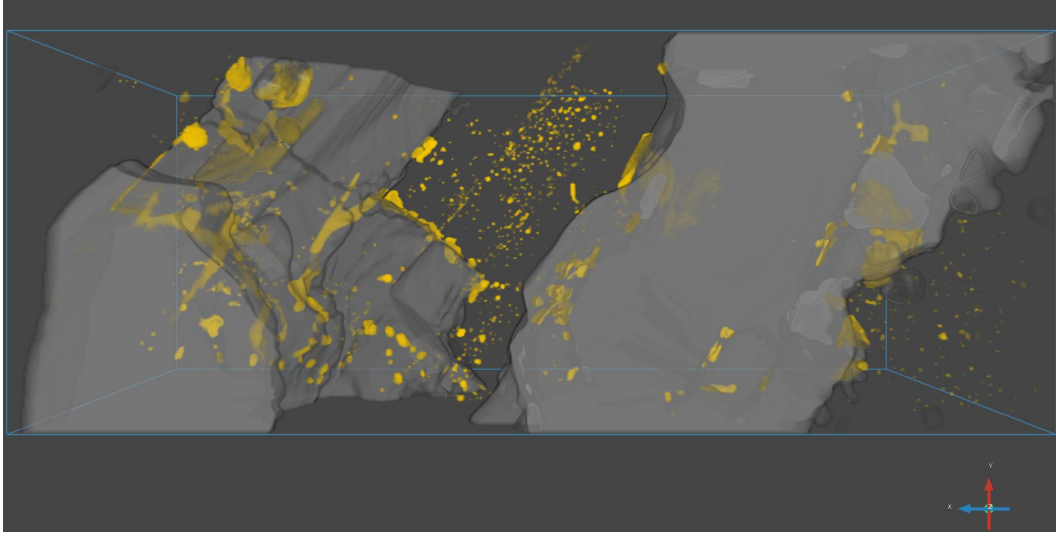


**Figure 2.** Overview of the  $26.2 \times 10.1 \times 10.5 \mu\text{m}^3$  volume exposed to the slice-and-view procedure with FIB-SEM. The large non-magnetic grains are indicated by a grayish color. The iron-oxides residing in this volume are indicated in yellow-brown. Note that iron-oxides in the center of the figure reside on the interfacial surfaces of plagioclase and pyroxene as well. Due to visibility, these large minerals were not imaged.

actively large minerals can be imaged properly using MicroCT, it allows for extrapolating the number of undetected small iron-oxides from the FIB-SEM analysis to the MicroCT data and hence produce a continuous grain-size distribution over both analyses.

Characterizing the mineral surface area (interfacial area) of the larger minerals, mainly plagioclase and pyroxene, required reprocessing the FIB-SEM data. Again, the original FIB-SEM dataset was binned and denoised using a non-local means filter. To calculate the mineral surface area, we applied a smoothing (median) filter to reduce small irregularities at mineral boundaries, while retaining overall shape (see Fig. S1b). Then we obtained the mineral surfaces by applying a K-means filter, and calculated the interfacial area by using a Lindblad-algorithm (Lindblad, 2005). The interfacial area consisted of about  $3.8 \times 10^6$  squared pixels that correspond to an area of  $\sim 1.53 \times 10^{-3} \text{ mm}^2$ . Fig. 2 shows the position of the mineral surface area together with the retrieved iron-oxides.

To calculate the mineral surface area in the MicroCT dataset, we started with the raw MicroCT data (DICOM files, available in repository of Out et al. (2023)) and reprocessed them using Dragonfly software by Object Research Systems (ORS). The Mi-

croCT data are rotated, cropped, and denoised with a non-local means filter, resulting into a scanned volume of  $1484 \times 33 \times 1425 \mu\text{m}^3$ . To image the interfacial area in the MicroCT data, we followed the same procedure as for the FIB-SEM data: a smoothing (median) filter was applied and the mineral surfaces were obtained through a K-means filter. After applying an edge detection filter to these groups, the interfacial area was calculated. This area determines by how much we need to scale the amount of iron-oxides retrieved from FIB-SEM data to the amount of iron-oxides retrieved from MicroCT data: the MicroCT interfacial area of  $4.00 \text{ mm}^2$  is approximately 2,620 times larger than the interfacial area retrieved from the FIB-SEM dataset. We therefore need to multiply the number of grains obtained from the FIB-SEM data by 2,620 to match the interfacial area of the MicroCT dataset. This resulted into a combined dataset of  $\sim 4.7 \times 10^6$  grains in the FIB-SEM realm and  $\sim 1.6 \times 10^3$  MicroCT iron-oxide grains. The FIB-SEM and MicroCT datasets can now be combined to produce a continuous grain-size distribution of iron-oxides for the entire range of interest (Fig. 3). The median grain-size has a diameter of 70 nm. From 30 to 70 nm the occurrence rapidly increases, after which the occurrence of grain diameters between 70 nm and  $10 \mu\text{m}$  follows a more gradually decaying trend.

All scripts used for the data processing of FIB-SEM data, the MicroCT data, and combining the two data-sets are available in a repository: Out et al. (2023). All choices made and parameters used are specified in these (Python) scripts.

### 2.3 Constructing the grain-size distribution

The trend in grain-size distribution can be described using a lognormal-like distribution between 20 nm and  $10 \mu\text{m}$ . We have chosen the lognormal distribution, because this distribution is frequently used to describe grain-sizes for e.g. magnetite powders (Smirnov, 2006; Yu et al., 2002). Nevertheless, the lognormal trend line was originally fitted to the logarithm with base 10 of the data. This logarithm ensures a better fit to grain-sizes larger than 70 nm. Through an iterative procedure reducing the least-squares error of our fit to the data, we found the best fitting distribution after which we transformed it back to linear space:

$$p = 3.51 * 10^{-6 + \frac{5.61}{d\sqrt{2\pi}}} \exp\left(-\frac{\ln^2(0.60d)}{6.29}\right) \text{ if } d : [0, 10] \quad (1)$$

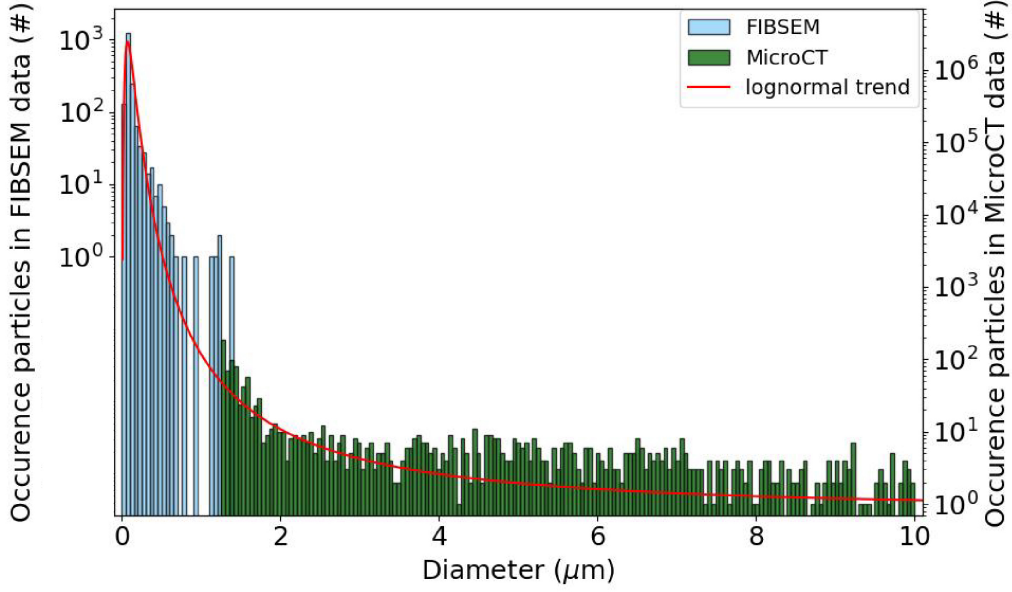


**Figure 3.** Overview of the non-normalized grain-size distribution. The histograms show the number of iron-oxides obtained from FIB-SEM or MicroCT data. The datasets are scaled to each other using interfacial area (see main text). The logarithmic trend line shows the fit to these scaled distributions.

with  $d$  the equivalent diameter of the iron-oxide grain in  $\mu\text{m}$  and  $p$  the probability density. Note that this probability density function, or pdf, is no longer a lognormal distribution, yet still accurately describes the data (Fig. 3). The function is only valid for grain-sizes between 0 and 10  $\mu\text{m}$ , although it could be extended to larger grain-sizes through rescaling.

To obtain a function from which grain-sizes can be sampled, the probability density function is integrated into a cumulative probability density function (cdf). This function takes a grain-size as input and returns the probability of finding that grain-size or smaller as output. Then to actually create a sampling function, this cdf has to be inverted. By inverting the function, a grain-size could be obtained as function of inputted cumulative probability. However, this inverted function has no analytical expression, so we created a look-up table to be able to sample the function. To create this table we inputted 100,000 diameters between 0 and 10  $\mu\text{m}$  into the cdf, which returned 100,000 cumulative probabilities. Each grain-size-probability pair was then put into the table. To sample grain-sizes from this look-up table we would generate a pool of random numbers, ob-

tained from a uniform distribution between 0 and 1 ( $U(0,1)$ ), equal to the number of samples requested. For each random number we would then extract the corresponding grain-size from the look-up table. Grain-sizes or probabilities not present in the table would be obtained through cubic interpolation of the nearest values. All Python codes to create and sample the grain-size distribution, and the look-up table are available in our repository (Out et al., 2023).

## 2.4 Validation

To obtain an independent verification for our method of combining FIB-SEM and MicroCT analyses, we validated our dataset through a scanning electron microscopy (SEM) image on a sister specimen from site HW03 (de Groot et al., 2013; ter Maat et al., 2018). Two areas of  $48.2 \times 71.3 \mu\text{m}^2$  and  $33.2 \times 49.0 \mu\text{m}^2$  within the sample were imaged with a resolution of 80 and 55 nm per 8-bit pixel respectively. After noise was removed, the images were thresholded to retrieve iron-oxides. Then the major axis  $m$  and minor axis  $n$  of each grain were determined and grain diameters,  $d$ , were calculated using (Yu et al., 2002):

$$d = 2\sqrt{m\frac{n}{\pi}} \quad (2)$$

The diameters of the grains were sorted to produce a normalized histogram with bin-sizes of  $0.1 \mu\text{m}$  ranging between  $0.2$  and  $3.0 \mu\text{m}$  - straddling the transition from the FIB-SEM realm to the MicroCT range. We discarded grains smaller than  $0.2 \mu\text{m}$  from the SEM data because they would be constructed from two pixels or less. On top of the SEM grain-size data, we overlaid the FIB-SEM and MicroCT normalized data (Fig. 4). The SEM data misses some of the smaller grains, as expected. The trends in the FIB-SEM+MicroCT and SEM datasets for grain-sizes  $>0.3 \mu\text{m}$ , however, correspond well. This shows that our method of combining FIB-SEM and MicroCT data gives a realistic description of the actual grain-size distribution of iron-oxides in our samples. A Kolmogorov-Smirnov test shows that the SEM distribution indeed underestimates the smaller grain-sizes with respect to the FIB-SEM–MicroCT dataset.

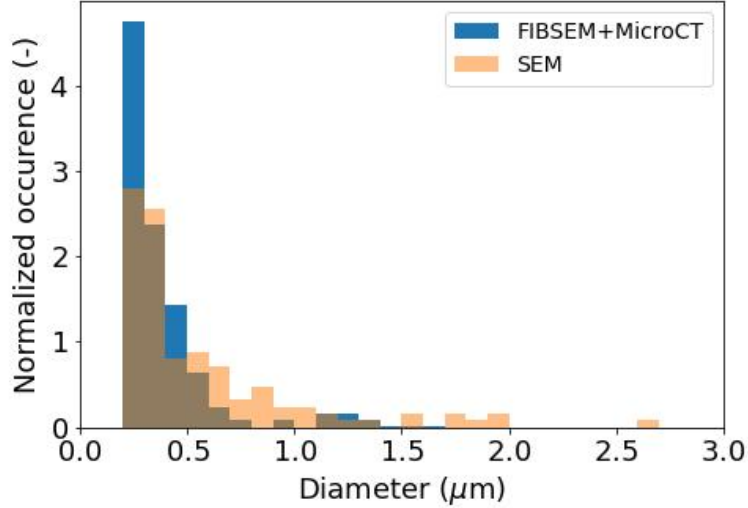


**Figure 4.** Verification of MicroCT and FIB-SEM data using separate SEM imaged iron-oxides using normalized histograms. Note that the distribution is similar for the two data-series except for the smallest grain-sizes.

### 3 Discussion

#### 3.1 Dataset limitations

For this study we used only one FIB-SEM sample that was taken from a specific, but typical Hawaiian lava flow. How well this sample represents the sample material of site HW03, let alone material from other sites, flows, and/or locations is a big unknown. Obtaining data from rock samples using FIB-SEM, however, is not a straightforward task; sample preparation, machine handling, and availability of resources complicate the scanning process. To get the most out of our data, we decided during initial phase of the FIB-SEM analyses to target an area with the highest amount of iron-oxides in view. This implies that relatively many small grains will be present in our FIB-SEM study, leading to an over-representation of small grains in our final grain-size distribution.

The overestimation, however, might be somewhat damped through our method of combining the FIB-SEM and MicroCT data through a scaling factor based on the interfacial areas of the larger minerals present in our sample. Our scaling factor is dependent on the amount of mineral surface area which scales with the number of grains and their volumes. This corrects for the in-homogeneous distribution of iron-oxides in the

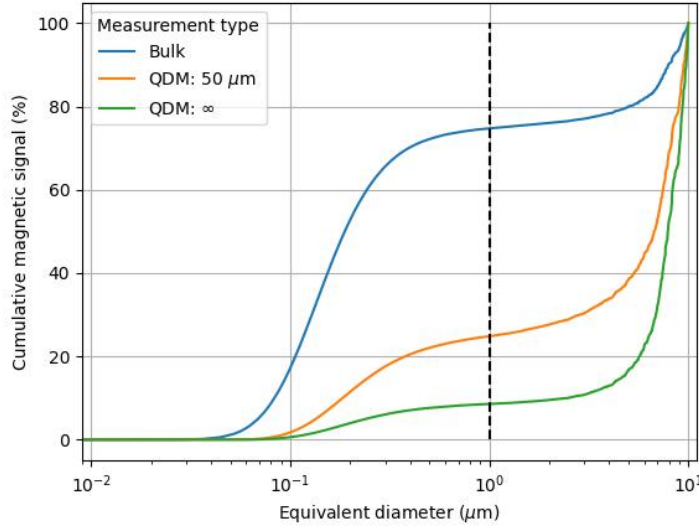


**Figure 5.** The cumulative magnetic signal of 10 million grains sampled from the grain-size distribution for measurements done with bulk sample magnetometers (blue) and scanning magnetometry (e.g. a QDM). For the QDM-geometries, we provide results for a ‘thick section’ with a layer of 50  $\mu\text{m}$  of sample (orange) and for a polished half space (green), both modeled with a sample-sensor distance of 5  $\mu\text{m}$ .

sample volume as shown by the FIB-SEM and MicroCT analyses. If we would use a scaling factor solely based on volume, the FIB-SEM volume would be scaled by a factor of 24,000 with respect to the MicroCT volume. This would most definitively result in a severe overestimation of grains imaged by FIB-SEM compared to grains imaged by MicroCT, because this volume scaling factor is one order of magnitude larger than our scaling factor based on the interfacial area of the larger minerals in our sample. We, therefore, consider scaling by grains per mineral interface area a stable protocol to ensure comparability between FIB-SEM and MicroCT results as it dampens local variations of the studied volume.

### 3.2 The contribution of magnetic signals as function of grain-sizes

#### 3.2.1 Measurements on bulk samples

The grain-size distribution for this specific sample from HW03 allows us to model magnetic contributions of iron-oxides as function of their grain-size in magnetic measure-



ments. First, we determine the contribution of the iron-oxides to the bulk magnetic moment of a sample as it would be measured using a cryogenic magnetometer or a Spinner. Therefore we sampled the grain-size distribution to obtain 10 million grains with diameters ranging from 20 nm to 10  $\mu\text{m}$ . Then we assigned magnetic moments to these grains based on their diameter following the trend line in Fig. 8.4 of Dunlop and Özdemir (1997). To obtain the magnetic moment as function of grain-size, we multiplied the magnetization as function of grain-size from this figure by the volume that a spherical grain with the specified diameter would have. All assigned magnetic moments have the same direction. This is an oversimplification of the reality and makes our analyses an end-member model emphasizing smaller grains fractions, as discussed below in section 3.2.3. To model the bulk magnetic moment of the total volume we summed the individual magnetic moments. The individual contribution of grains as function of their grain-size was calculated by cumulatively summing the individual magnetic moments, and dividing by the resulting bulk magnetic moment (blue line Fig. 5).

### 3.2.2 *Implications for scanning magnetometry*

In scanning magnetometry, the geometry between the iron-oxide grains and the measurement sensors differs from the geometry when measuring bulk samples. The sensors, or in case of the QDM the layer of NV-centers, are much closer to the individual grains and the distance between the measurement plane and individual grains differs between grains. Often a sensor-sample distance of only 5  $\mu\text{m}$  is achievable in a QDM set-up. When correcting the trend in Fig. 8.4 of Dunlop and Özdemir (1997) for grain volumes and calculating the magnetic moment as function of grain-size it becomes apparent that larger grains have a higher magnetic moment than smaller grains, although the magnetization of the smaller grains is higher than the magnetization of larger grains. Larger grains are therefore better visible for the QDM than smaller grains at the same distance from a magnetic sensor (see also the discussion in de Groot et al. (2021)).

To model the contributions of individual magnetic moments on measurements obtained with a QDM, we start with the same 10 million grains and their assigned magnetic moments that were sampled from our grain-size distribution to calculate the magnetic moment of a bulk sample. The magnetic moments are in the z-direction: normal to the measurement plane with the NV centers. We investigate the individual contribution of magnetic carriers here for two different QDM samples. First, we simulated a ‘thick

section' with a sample layer with a thickness of  $50\text{ }\mu\text{m}$  as is often used for MMT experiments. Second, we assess the geometry of a polished half space: a sample with an 'infinite' thickness – below we show that a thickness of  $250\text{ }\mu\text{m}$  is enough to loose the signal of all grains  $<10\text{ }\mu\text{m}$  below the typical noise level of the QDM. For both simulations we used a typical minimum distance to the NV centers (sample-sensor distance, or depth) of  $5\text{ }\mu\text{m}$ .

For our thick section we assign our 10 million grains as described above a depth in the sample at random between 5 and  $55\text{ }\mu\text{m}$  depth. Then we cumulatively summed the magnetic moments of only those grains which produce a magnetic signal at the sensor surpassing a noise level of 5 nT (lower limit of the noise level of the QDM according to Glenn et al., 2017). Then we normalized the cumulative magnetic moment as function of grain-size to the total magnetic moment of all grains visible in the QDM scan (orange line Fig. 5).

For the polished half space we used a slightly different approach; for each grain-size we calculated the minimum depth at which a grain is no longer visible above the background noise in the QDM (5 nT), with a minimum sample-sensor distance of  $5\text{ }\mu\text{m}$ . Then we normalized by the depth at which the magnetic signal of an iron-oxide grain with a diameter of  $10\text{ }\mu\text{m}$  is equal to the background noise. This corresponds to a distance of  $\sim 250\text{ }\mu\text{m}$  to sensor. This normalization makes the depth per grain-size trend independent of noise level (Fig. S2). Per grain diameter, this normalized depth is multiplied with the corresponding magnetic moment. Similar to the bulk magnetic moment, these 'weighted' moments are summed to obtain a weighted bulk magnetic moment representative for the QDM; the contributions per diameter are calculated by cumulatively summing the individual weighted magnetic moments and are divided by the weighted bulk magnetic moment (green line in Fig. 5).

The simulations for the three sample geometries show that the measurements are dominated by different grain-size fractions. Bulk sample measurements emphasize smaller grains:  $\sim 50\%$  of the signal arises from iron-oxides  $<200\text{ nm}$ , and  $>75\%$  from grains  $<1\text{ }\mu\text{m}$ . For typical MMT samples with a thickness of  $50\text{ }\mu\text{m}$ , only 25% of the cumulative magnetic signal in a QDM scan originates from grains  $<1\text{ }\mu\text{m}$ . The contribution of grains  $<1\text{ }\mu\text{m}$  drops even further, to  $<10\%$ , for a polished half space for QDM measurements.

### 3.2.3 Limitations of our simulations

In our simulations we assigned all grains a magnetic moment in the same direction. This is obviously an oversimplification in our model since we ignore the efficiency with which different grain-sizes can capture the magnetic field. For SD grains only  $\sim 2\%$  align with the magnetic field (Berndt et al., 2016). For larger grain-sizes it is unknown which fraction aligns with the imparting field, although this may very well be (much) higher than  $2\%$  (e.g. Nagy et al., 2017). This means that we favor small, SD, grains in our analyses, since we assign them all a magnetic moment in the same direction, i.e. an efficiency in reproducing the imparting field’s direction of 100%. We therefore most likely overestimate the contributions of the smaller grain-sizes in the cumulative magnetic signal in Fig. 5, and the trend lines should therefore be interpreted as an end-member. It is very likely that the real trend lines for these three sample geometries is skewed more to the right, allocating a larger part of the cumulative signal to larger grain-size fractions. The lack of a proper understanding of the efficiency of larger grain-sizes to align themselves with the imparting magnetic field when they acquire their magnetization currently hampers a better simulation of the cumulative magnetic signal in our sample.

### 3.3 Implications for Micromagnetic Tomography studies

The cumulative magnetic signal as function of grain-size in Fig. 5 allows us to put MMT studies in which ghost grains are present into perspective. The first MMT studies were based on synthetic samples in which the grain-size distribution was controlled (e.g. (most) results in de Groot et al., 2018, 2021). For these synthetic samples, the iron-oxide grains were sieved so that only grains that are well above the MicroCT resolution were present. The natural basalt samples used by de Groot et al. (2021) and Kusters et al. (2023), however, undoubtedly contain many undetected ghost grains. Both studies assess the magnetic moment of iron-oxides detected by MicroCT in a  $30\text{ }\mu\text{m}$  thin section of Hawaiian basaltic rock from site HW03, which is a sister-specimen to the sample subjected to our study. The resolution of the MicroCT used in those studies allows detecting grains with a diameter  $\sim 1\text{ }\mu\text{m}$ . Since 1,646 grains were isolated from the MicroCT data by Kusters et al. (2023) the grain-size distribution reported here (Fig. 3) implies the existence of almost 5 million undetected ghost grains in their sample – or  $\sim 3,000$  ghost grains per detected iron-oxide grain. Remarkably, both de Groot et al. (2021) and Kusters et al. (2023), were capable of obtaining realistic magnetic moments for the de-

tected iron-oxide grains, and their results are interpretable in terms of magnetic moment and direction. Also, reported trends as function of grain-size and magnetic treatment follow expectations based on earlier work (e.g. Dunlop & Özdemir, 1997).

Given the resolution of the MicroCT, grains with a diameter  $<1\ \mu\text{m}$  most likely go undetected and are thus ghost grains. The cumulative magnetic signal (Fig. 5) reveals that, even though they are high in number, these ghost grains in a sample from HW03 only contribute to at most 25% of the total measured signal from a typical sample for a QDM scan. More than 75% of the signal in a QDM scan arises from grains  $>1\ \mu\text{m}$ . For thicker samples, such as polished surfaces, this increases to over 90% of the signal. Their contribution therefore may be unintuitively low compared to the contributions of these small grain-size fractions to bulk sample measurements.

Nevertheless, the magnetic signals from ghost grains in an MMT inversion are a potential source of error: these signals are present in the QDM scan, but their sources are not known. Since the ghost grains are small, the spatial extent of their signals in a QDM scan is limited. Moreover, the directions of the magnetic moments from ghost grains are not uniform: SD grains for example only have a 2% preference of aligning their magnetic moments with the imparting magnetic field when acquiring their magnetization (Berndt et al., 2016). As ghost grains are also high in number, we hypothesize that the total contribution of these grains in the QDM scan effectively becomes unbiased noise for the MMT inversion. Lastly, MMT inversions are generally vastly overdetermined, i.e. the number of data points in the QDM scans are generally many times higher than the amount of variables to solve for in the system. This makes the inversion resistant to the presence of noise in the magnetic surface scan. All this combined explains why MMT studies are capable of solving magnetic moments of many grains in a sample that are detected by the MicroCT, in spite of the presence of many more ghost grains that go undetected.

Lastly, it is important to emphasize once more that our simulation of the cumulative magnetic signal as function of grain-size emphasizes, and presumably overestimates, the contribution of small grains. This implies that the scenario presented here is an end-member scenario for MMT: most likely the cumulative contribution is skewed towards larger grains, and small grains contribute even less to scanning magnetometry measurements. This would be even more favorable for MMT studies.

### 3.4 Implications for (paleointensity) measurements on bulk samples

A micromagnetic modeling study by Nagy et al. (2017) characterised the magnetic behavior as function of increasing grain-sizes from the superparamagnetic threshold at 40 nm, through different vortex states in grains >150 nm. They identified the following micromagnetic behavior in increasingly larger grains: SD between 40 and 60 nm, ‘flower’ states between 60 and 80 nm, ‘hard-axis-aligned vortex’ between 80 and 100 nm, and ‘easy-axis-aligned vortex’ for grains >100 nm (with an upper limit in this study of ~150 nm). The hard-axis-aligned vortex state is very susceptible to losing their (imparted) magnetic moment due to low unblocking temperatures, also on laboratory time-scales (c.f. Fig. 3 in Nagy et al. (2017)). This would potentially hamper paleomagnetic experiments that require reheating samples, such as traditional intensity techniques.

In our grain-size distribution for site HW03, about 10% of the bulk magnetic signal is carried by the specific grain-size range of the hard-axis-aligned vortex state between 80 and 100 nm (Fig. 5), although we have to keep in mind that our simulations most likely favor the contributions of small grains. Nevertheless, we hypothesize that it may be possible to attribute (some of) the low success rates of paleointensity experiments on samples that otherwise look ideal (e.g. no signs of thermal alteration during the experiments, relatively pure magnetite carriers, no low-temperature overprints, etc) by a relatively large presence of grains with these disruptive hard-axis-aligned vortex states.

### 3.5 Comparing measurements on bulk samples with magnetic surface scans

The cumulative magnetic signal as function of grain-size in Fig. 5 also has implications for how well bulk sample measurements and surface magnetometry measurements obtained from the same sample (or sister samples) are comparable. For our sample, sub-micron grains determine only 10 to 25% of the total signal in QDM measurements, but they make up >75% of the magnetic signal in bulk measurements. This implies that the magnetic signal as measured on bulk samples largely arises from a different grain-size fraction, i.e. magnetic carriers, inside the sample than the signal that is measured in scanning magnetometry. This prevents a reliable and straightforward one-to-one comparison of the magnetic behavior as observed in bulk samples and in scanning magnetometry in samples with grain-size distributions comparable to the one we found for site HW03.

## 486 4 Conclusions

487 Here we produced a grain-size distribution of all stable iron-oxides larger than the  
 488 superparamagnetic threshold in an Hawaiian basalt by combining MicroCT and FIB-  
 489 SEM data of sister-specimens. The MicroCT and FIB-SEM datasets were scaled using  
 490 the interfacial area of large, non-iron-oxide, minerals present in the sample (i.e. honey-  
 491 comb structure), because iron-oxides tend to cluster on the edges of large minerals in the  
 492 studied specimen. Through this scaling procedure we have created a lognormal-like dis-  
 493 tribution between 20 nm to 10  $\mu\text{m}$  that spans the range of stable SD, PSD, and MD iron-  
 494 oxides.

495 We used this grain-size distribution to assess the influence of grain-sizes on both  
 496 bulk sample magnetic measurements and scanning magnetometry results. We found that  
 497 measurements on bulk samples are sensitive to small grain-sizes; in our sample  $\sim 50\%$   
 498 of the bulk magnetic measurement arises from grains  $< 200$  nm, and  $75\%$  from grains  $< 1$   
 499  $\mu\text{m}$ . Scanning magnetometry results such as QDM scans are governed by larger grains  
 500 in the sample:  $75$  to  $90\%$  of the measured signals arise from grains  $> 1$   $\mu\text{m}$ .

501 Our observations imply that caution is necessary when bulk sample magnetic mea-  
 502 surements are compared to scanning magnetometry results acquired from the same sam-  
 503 ple (material). The magnetic carriers that are actually measured in both techniques may  
 504 very well differ, certainly in size, but possibly also in chemistry and mineralogy. Lastly,  
 505 our observations are reassuring for MMT results derived from volcanic rocks: the ma-  
 506 jority of the signals arises from grains that are large enough to be reliably imaged us-  
 507 ing MicroCT, and the contributions of ghost grains are limited.

## 508 Data availability statement

509 The FIB-SEM, MicroCT, and SEM data used for obtaining and verifying, and the  
 510 jupyter notebooks employed for generating the grain-size distribution and honeycomb  
 511 structure in this study are available at YODA via <https://doi.org/10.24416/UU01-QNASXB>  
 512 with a CC-BY-NC-4.0 license (Out et al., 2023). Numerical calculations were executed  
 513 with support of NumPy (Harris et al., 2020), SciPy (Virtanen et al., 2020), OpenCV (Bradski,  
 514 2000), and Matplotlib (Hunter, 2007) Python libraries. The MicroCT analysis for this  
 515 study was generated using Dragonfly software, Version 2022.1.0.1259 for Windows. Ob-  
 516 ject Research Systems (ORS) Inc, Montreal, Canada, 2022.

## Acknowledgments

We want to thank our two anonymous reviewers for their constructive comments on an earlier version of this manuscript, which provided new insights and significantly helped to improve our study. This project has received funding from the European Research Council (ERC) under the European Union’s Horizon 2020 research and innovation program (Grant agreement No. 851460 to L.V. de Groot). This publication results from work carried out under transnational access action under the support of EXCITE – EC- HORIZON 2020 – INFRAIA 2020 Integrating Activities for Starting Communities (Grant agreement No. 101005611).

## References

- Berndt, T., Muxworthy, A. R., & Fabian, K. (2016). Does size matter? statistical limits of paleomagnetic field reconstruction from small rock specimens. *Journal of Geophysical Research: Solid Earth*, *121*(1), 15–26. doi: 10.1002/2015JB012441
- Bradski, G. (2000). The OpenCV Library. *Dr. Dobbs’s Journal of Software Tools*.
- de Groot, L. V., Biggin, A. J., Dekkers, M. J., Langereis, C. G., & Herrero-Bervera, E. (2013, 12). Rapid regional perturbations to the recent global geomagnetic decay revealed by a new Hawaiian record. *Nature Communications*, *4*(1), 2727. doi: 10.1038/ncomms3727
- de Groot, L. V., Fabian, K., Béguin, A., Kesters, M. E., Cortés-Ortuño, D., Fu, R. R., ... Barnhoorn, A. (2021). Micromagnetic tomography for paleomagnetism and rock-magnetism. *Journal of Geophysical Research: Solid Earth*, *126*(10). doi: 10.1029/2021JB022364
- de Groot, L. V., Fabian, K., Béguin, A., Reith, P., Barnhoorn, A., & Hilgenkamp, H. (2018). Determining individual particle magnetizations in assemblages of micrograins. *Geophysical Research Letters*, *45*(7), 2995–3000. doi: 10.1002/2017GL076634
- Dunlop, D. J., & Özdemir, Ö. (1997). *Rock Magnetism*. Cambridge University Press. doi: 10.1017/cbo9780511612794
- Einsle, J. F., Harrison, R. J., Kasama, T., Conbhuí, P. Ó., Fabian, K., Williams, W., ... Midgley, P. A. (2016). Multi-scale three-dimensional characterization of iron particles in dusty olivine: Implications for paleomagnetism



- of chondritic meteorites. *American Mineralogist*, 101(9), 2070–2084. doi: 10.2138/am-2016-5738CCBY
- Fabian, K., & De Groot, L. V. (2019, 2). A uniqueness theorem for tomography-assisted potential-field inversion. *Geophysical Journal International*, 216(2), 760–766. doi: 10.1093/gji/ggy455
- Glenn, D. R., Fu, R. R., Kehayias, P., Le Sage, D., Lima, E. A., Weiss, B. P., & Walsworth, R. L. (2017, 8). Micrometer-scale magnetic imaging of geological samples using a quantum diamond microscope. *Geochemistry, Geophysics, Geosystems*, 18(8), 3254–3267. doi: 10.1002/2017GC006946
- Harris, C. R., Millman, K. J., van der Walt, S. J., Gommers, R., Virtanen, P., Cournapeau, D., . . . Oliphant, T. E. (2020, 9). Array programming with NumPy. *Nature*, 585(7825), 357–362. doi: 10.1038/s41586-020-2649-2
- Hunter, J. D. (2007, 5). Matplotlib: A 2D Graphics Environment. *Computing in Science & Engineering*, 9(3), 90–95. doi: 10.1109/MCSE.2007.55
- Kosters, M. E., de Boer, R. A., Out, F., Cortés-Ortuño, D. I., & de Groot, L. V. (2023). Unraveling the magnetic signal of individual grains in a hawaiian lava using micromagnetic tomography. *Geochemistry, Geophysics, Geosystems*, 24(4). doi: 10.1029/2022GC010462
- Lindblad, J. (2005). Surface area estimation of digitized 3d objects using weighted local configurations. *Image and Vision Computing*, 23(2), 111–122. doi: 10.1016/j.imavis.2004.06.012
- Nagy, L., Williams, W., Muxworthy, A. R., Fabian, K., Almeida, T. P., Conbhui, P. O., & Shcherbakov, V. P. (2017). Stability of equidimensional pseudo-single-domain magnetite over billion-year timescales. *Proceedings of the National Academy of Sciences of the United States of America*, 114(39), 10356–10360. doi: 10.1073/pnas.1708344114
- Nikolaisen, E. S., Harrison, R. J., Fabian, K., & McEnroe, S. A. (2020). Hysteresis of natural magnetite ensembles: Micromagnetics of silicate-hosted magnetite inclusions based on focused-ion-beam nanotomography. *Geochemistry, Geophysics, Geosystems*, 21(11). doi: 10.1029/2020GC009389
- Out, F., Cortés-Ortuño, D., Fabian, K., van Leeuwen, T., & de Groot, L. V. (2022). A first-order statistical exploration of the mathematical limits of micromagnetic tomography. *Geochemistry, Geophysics, Geosystems*. doi:

- 10.1029/e2021GC010184
- Out, F., de Boer, R. A., Walmsley, J., & de Groot, L. V. (2023). *Replication Data for: Modeling the Distribution of Iron-oxides in Basalt by combining FIB-SEM and MicroCT Measurements*. YODA. doi: 10.24416/UU01-QNASXB
- Smirnov, A. (2006). Memory of the magnetic field applied during cooling in the low-temperature phase of magnetite: Grain size dependence. *Journal of Geophysical Research: Solid Earth*, 111(B12). doi: 10.1029/2006JB004573
- Tauxe, L., & Yamazaki, T. (2015). Paleointensities. In *Treatise on geophysics* (pp. 461–509). Elsevier. doi: 10.1016/B978-0-444-53802-4.00107-X
- ter Maat, G. W., Pennock, G. M., & de Groot, L. V. (2018). Data descriptor: A chemical, crystallographic and magnetic characterisation of individual iron-oxide grains in Hawaiian lavas. *Scientific Data*, 5, 1–9. doi: 10.1038/sdata.2018.162
- Virtanen, P., Gommers, R., Oliphant, T. E., Haberland, M., Reddy, T., Cournapeau, D., . . . van Mulbregt, P. (2020, 3). SciPy 1.0: fundamental algorithms for scientific computing in Python. *Nature Methods*, 17(3), 261–272. doi: 10.1038/s41592-019-0686-2
- Yu, Y., Dunlop, D. J., & Özdemir, Ö. (2002). Partial anhysteretic remanent magnetization in magnetite 1. additivity. *Journal of Geophysical Research: Solid Earth*, 107(B10), EPM–7. doi: 10.1029/2001JB001249